Sensors & Diagnostics

PAPER

View Article Online
View Journal | View Issue

Open Access Article. Published on 06 October 2023. Downloaded on 2/10/2026 7:54:17 PM.
This article is licensed under a Creative Commons Attribution-NonCommercial 3.0 Unported Licence.

Check for updates

Cite this: *Sens. Diagn.*, 2023, **2**, 1585

# A Zn-MOF functionalized with alkyne groups: ultrasensitive detection of $Cu^{+}$ and $Pd^{2+}$ ions in aqueous medium†

Aashish, Ruchika Gupta and Rajeev Gupta *

Received 20th July 2023,
Accepted 6th October 2023

DOI: 10.1039/d3sd00188a

rsc.li/sensors

An alkyne-functionalized Zn(II)-based luminescent metal–organic framework (MOF) **1** has been synthesized and structurally characterized. MOF **1** functions as an ultrasensitive and ultrafast chemosensor for the 'turn-off' detection of $Cu^{+}$ and $Pd^{2+}$ ions in an aqueous medium. MOF **1** exhibits not only an extremely low detection limit of 53 and 71 nM for $Cu^{+}$ and $Pd^{2+}$ ions, respectively, but also an ultrafast response time of *ca.* 10 s. The emission quenching in **1** is attributed to FRET due to the interaction of alkyne–π bonds with the d-orbitals of soft $Cu^{+}$ and $Pd^{2+}$ ions. Such a π–d interaction was confirmed by the solid-state NMR and FTIR spectral studies, XPS studies, zeta potential measurements and EDX analyses. To further validate the role of the alkyne group in controlling the said interaction in MOF **1**, its structural analogue MOF **2** but carrying a saturated alkyl group was synthesized and structurally characterized. MOF **2** failed to recognize both $Cu^{+}$ and $Pd^{2+}$ ions, thus confirming a critical role of the alkyne group in participating in the interaction with the $Cu^{+}$ or $Pd^{2+}$ ions *via* the propargyl group of MOF **1** which resulted in fluorescence quenching *via* a dynamic quenching pathway. MOF **1** selectively detects both $Cu^{+}$ and $Pd^{2+}$ ions in different water samples as well as in the presence of other interfering metal ions, while MOF-based paper strips are used for real-life monitoring.

## Introduction

Metal–organic frameworks (MOFs) are a significant class of tunable materials with large surface area, high porosity, high crystallinity, and remarkable structural features.[1–4] MOFs have emerged as promising materials for a number of applications including gas adsorption,[5,6] storage and separation,[7,8] proton and hydroxide conduction,[9,10] sensing,[11,12] imaging and optics,[13,14] heterogeneous catalysis,[15–17] and magnetism.[18] Through a judicious selection of organic linkers and metal ions/nodes/clusters,[19] assorted MOFs featuring diverse topologies and properties could be rationally constructed.[20] Out of various MOFs, the luminescent ones are significant due to their valuable applications in the fields of sensing,[11,12] imaging and optics.[13,14] Here, selection of an organic linker is critical for the design of luminescent MOFs for specific detection applications.[21,22] For example, functionalized organic linker(s) in a MOF can selectively and reversibly interact with a specific analyte.[23] Utilizing such design strategies, various luminescent MOFs have been developed for the selective sensing of metal ions,[24,25] anions,[26,27] small organic molecules,[28] explosives,[29] biological signalling molecules,[30] ROS,[31] and even drugs.[32]

Transition metals are essential for living organisms, including humans, due to their involvement in numerous cellular processes.[33–35] Copper, the third most abundant essential element in humans, is involved in various biological and metabolic processes.[34,36] Inside a cell, copper switches between the cupric ($Cu^{2+}$) and cuprous ($Cu^{+}$) forms.[37] However, due to cytosol's reducing environment, copper typically exists in the cuprous form inside a cell.[38] While development of a fluorescent sensor for the cupric form is relatively easy, detection of cuprous ions is rather challenging.[37,39] As a result, many fluorescent chemosensors have been developed for cupric ions, and sensing of cuprous ions is very sparse.[40–43] Thus, it is crucial to develop fluorescent chemosensors for the sensitive and selective detection of cuprous ions, preferably under biologically relevant conditions.[41,42]

The palladium metal is extensively used for various chemical, industrial and medical applications.[44–48] The excessive use of palladium inevitably leads to environmental contamination and has a detrimental impact on both flora and fauna, including humans.[49,50] The ability of palladium to undergo complexation with different biomolecules raises serious concerns, even when present in minute concentrations.[51,52] Thus, it is quite essential but a challenging task to design a chemosensor that can selectively detect Pd ions.

*Department of Chemistry, University of Delhi, Delhi 110 007, India.*
*E-mail: rgupta@chemistry.du.ac.in; Web: https://people.du.ac.in/~rgupta/*

† Electronic supplementary information (ESI) available. CCDC 2282500–2282501. For ESI and crystallographic data in CIF or other electronic format see DOI: https://doi.org/10.1039/d3sd00188a

© 2023 The Author(s). Published by the Royal Society of Chemistry

Open Access Article. Published on 06 October 2023. Downloaded on 2/10/2026 7:54:17 PM.
This article is licensed under a Creative Commons Attribution-NonCommercial 3.0 Unported Licence.

Although diverse ranges of fluorescent chemosensors have been developed based on small organic molecules,[53,54] organic polymers,[55,56] inorganic–organic hybrids,[57,58] and quantum dots,[59,60] their low water stability and poor reusability hinder their applicability for real-life applications.[61,62] In this context, the stable and robust nature of MOFs can circumvent the aforementioned drawbacks.[19] In particular, luminescent MOFs have the ability to act as multifunctional fluorescent chemosensors for the selective and sensitive detection of assorted analytes.[63]

Both $Cu^+$ and $Pd^{2+}$ ions fall under the category of soft metals and therefore the design aspect must incorporate functional groups that are known to interact with soft metals.[64,65] In this context, an alkyne functional group is well known to interact with soft metals due to its good $\pi$-donor capability which allows overlap with metal's vacant d-orbitals.[66,67] Therefore, incorporation of an alkyne functional group within a luminescent MOF would be an ideal strategy.[68] Moreover, the thermal stability and chemical robustness as well as the porous nature of MOFs will be additional advantages.[3]

Herein, we report the design and synthesis of an alkyne-functionalized Zn(II)-based MOF (**1**) for the ultrasensitive detection of $Cu^+$ and $Pd^{2+}$ ions. The fluorescence spectral studies illustrate that **1** selectively detects both $Cu^+$ and $Pd^{2+}$ ions with an extremely low detection limit and a fast response *via* the emission turn-off effect. We provide convincing evidence that both $Cu^+$ and $Pd^{2+}$ ions interact with the alkyne groups of the Zn-MOF *via* soft···soft interactions. An important feature is that the entire sensing is performed in an aqueous medium, thus highlighting its significance. A structural analogue of **1**, however, functionalized with a saturated propyl group (MOF **2**), was incapable of recognizing both $Cu^+$ and $Pd^{2+}$ ions. Such a fact provides structural evidence for confirming the actual binding site, the alkyne groups, in MOF **1**. MOF **1** is also capable of selectively detecting $Cu^+$ and $Pd^{2+}$ ions in different water samples as well as in the presence of other interfering metal ions, while MOF-based paper strips are used for real-life monitoring. To the best of our knowledge, this is the first report for the detection of $Cu^+$ ions in an aqueous medium under the regime of MOFs.

## Results and discussion

### Synthesis and characterization of Zn-MOF 1

Ligand **L3** (Fig. S1–S9, ESI†) was synthesized in two steps starting from **L1** (Scheme 1). Ligand **L3**, functionalized with an alkyne group, offers two arylcarboxylic acid groups with the potential to coordinate suitable metal ions. **L3** upon reaction with $Zn(OAc)_2$ resulted in the formation of three-dimensional (3D) Zn(II)-MOF **1** (Scheme 1). In the FTIR spectrum, **1** exhibited strong stretching at 1675–1590 $cm^{-1}$ corresponding to both $\nu_{COO}$ and $\nu_{C=O}$ groups (Fig. S10, ESI†).[69] MOF **1** also displayed broad $\nu_{O-H}$ stretching at 3370–3210 $cm^{-1}$ due to the presence of lattice water molecules while a strong band at *ca.* 1027 $cm^{-1}$ is indicative of lattice DMSO. The FTIR spectrum of **1** also showed stretching at 3321 and 2122 $cm^{-1}$ corresponding to $\nu_{C\equiv C-H}$ and $\nu_{C\equiv C}$ groups, respectively, thus confirming the presence of appended propargyl groups.[69] TG analysis of **1** suggested its good thermal stability (*ca.* 300 °C) after showing weight changes for the loss of lattice DMSO and water molecules (Fig. S11, ESI†). The elemental composition of **1** was confirmed by using energy dispersive X-ray (EDX) spectroscopy (Fig. S12, ESI†). The PXRD pattern of as-synthesised **1** closely matched with the one simulated from the single crystal X-ray diffraction analysis, indicating the phase purity of the bulk material (Fig. S13, ESI†). The chemical stability of MOF **1** was investigated by soaking it in an aqueous solution of different pH values (4, 5, and 9) and a range of organic solvents (methanol, acetone, chloroform, and hexane) (Fig. S14, ESI†).

The PXRD studies explicitly illustrated that both the crystallinity and framework integrity of MOF **1** were well preserved in both aqueous solutions of different pH values and solvents of varying polarities. These studies strongly evidence that MOF **1** is chemically robust and can be utilized for various applications.

MOF **1** was crystallographically characterized to understand its 3D molecular architecture. Details of the X-ray data collection and structure solution parameters are provided in Table S1, whereas Tables S2 and S3† contain selected bonding parameters. The diffraction studies revealed that MOF **1** crystallized in a monoclinic cell with the *C*2/*C* space group.

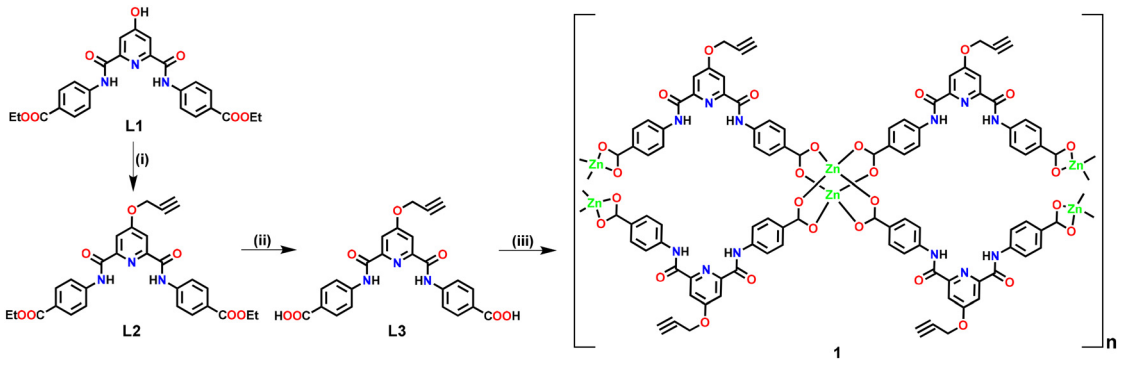


**Scheme 1** Preparative route for the synthesis of Zn(II)-MOF **1**. Reaction conditions: (i) propargyl bromide, $K_2CO_3$; (ii) $OH^-$; (iii) $Zn(OAc)_2$.

 © 2023 The Author(s). Published by the Royal Society of Chemistry

Open Access Article. Published on 06 October 2023. Downloaded on 2/10/2026 7:54:17 PM.
This article is licensed under a Creative Commons Attribution-NonCommercial 3.0 Unported Licence.

The asymmetric unit consists of one ligand **L3** (in its dianionic form), one $Zn^{2+}$ ion, and one molecule each of water and DMSO in the crystal lattice (Fig. 1(a)). The overall two negative charges of the dianionic ligand are balanced by the dicationic zinc ion. The secondary building unit (SBU) of **1** consists of four arylcarboxylate groups emanating from four different ligands and two Zn(II) ions forming a paddle-wheel core, $[Zn_2(-COO)_4]$. In the SBU, both $Zn^{2+}$ ions adopted a distorted tetrahedral geometry, where the two zinc ions are separated by 2.95 Å (Fig. 1(b)). Such SBUs are connected together to generate a 3D architecture (Fig. 1(c)–(f)). MOF **1** exhibited the presence of large open pores with dimensions of 17.39 × 16.20 $Å^2$ (Fig. 1(c)). Such an observation was satisfactorily supported by the Brunauer–Emmett–Teller (BET) studies which revealed pores of *ca.* 1.5 nm dimensions and a surface area of 10.29 $m^2$ $g^{-1}$ (Fig. S15, ESI†).[70] Notably, such pores are lined with the functionalized propargyl groups. Such a fact provides a unique opportunity for the recognition and binding of a specific analyte within the porous structure of **1** (*vide infra*).

### Sensing studies

The emission spectra of **1** were recorded in a variety of solvents as its suspensions: MeCN, $CHCl_3$, THF, MeOH, EtOH, $H_2O$, acetone, toluene, DMF, DMSO, ethylene glycol, nitromethane and nitrobenzene (Fig. S16, ESI†). However, water was found to be the best solvent in terms of high emission

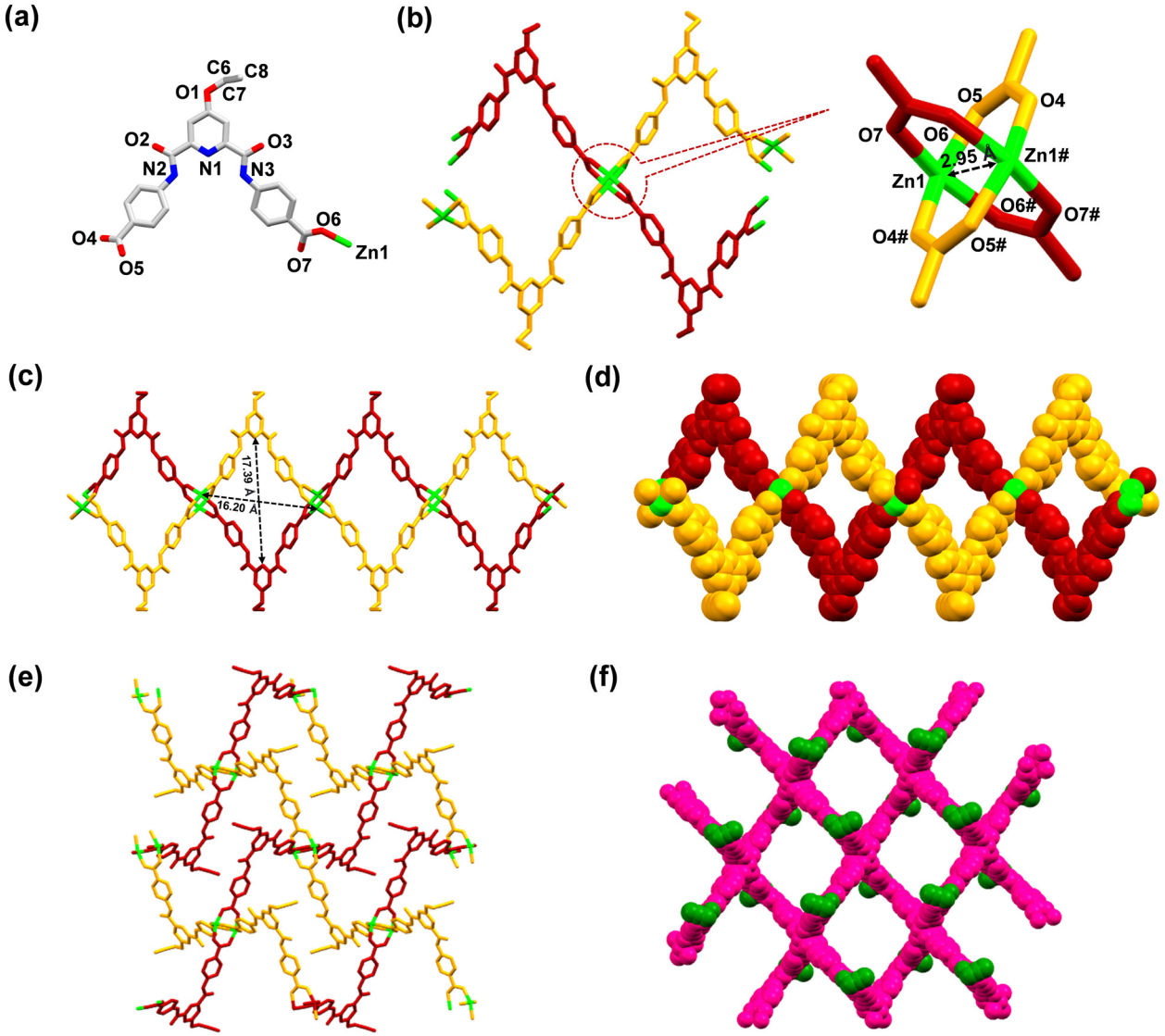


**Fig. 1** (a) Asymmetric unit of MOF **1**; colour codes: green, Zn; blue, N; red, O; grey, C. Lattice water and DMSO molecules and hydrogen atoms have been omitted for clarity. (b) Partial crystal structure of **1** showing the coordination environment around the $Zn^{2+}$ centers. (c) A view of the 3D network of **1** displaying the cavity structure and its dimensions, when viewed along the *b*-axis. (d) Space-filling diagram of **1**, when viewed along the *b*-axis. (e) A view of the 3D network of **1**, when viewed along the *a*-axis. (f) Space-filling diagram of **1**, where propargyl groups are shown in green colour for distinction, when viewed along a perpendicular axis to the *bc* plane.

Open Access Article. Published on 06 October 2023. Downloaded on 2/10/2026 7:54:17 PM.
This article is licensed under a Creative Commons Attribution-NonCommercial 3.0 Unported Licence.

intensity of **1** and its real-life applicability.[71] Therefore, all subsequent studies were performed in an aqueous medium. The suspension of MOF **1** in $H_2O$ displayed a prominent emission with a maximum at 435 nm upon excitation at 325 nm. In fact, the solid-state fluorescence spectrum of **1** also exhibited an intense emission band at 435 nm (Fig. S17, ESI†). Subsequently, the emission spectra of **1** were investigated after the addition of assorted metal ions such as $Hg^{2+}$, $Pt^{2+}$, $Cu^{2+}$, $Ag^{+}$, $Pb^{2+}$, $Co^{2+}$, $Zn^{2+}$, $Cd^{2+}$, $Mg^{2+}$, $Cr^{3+}$, $Ni^{2+}$, $Mn^{2+}$, $Na^{+}$, $K^{+}$, $Al^{3+}$, and $Fe^{2+}$. Importantly, the addition of these metal ions to an aqueous suspension of MOF **1** did not significantly perturb its emission intensity. However, in the presence of both $Cu^{+}$ and $Pd^{2+}$ ions, the emission intensity of **1** was significantly quenched (Fig. 2(a)). The presence of $Cu^{+}$

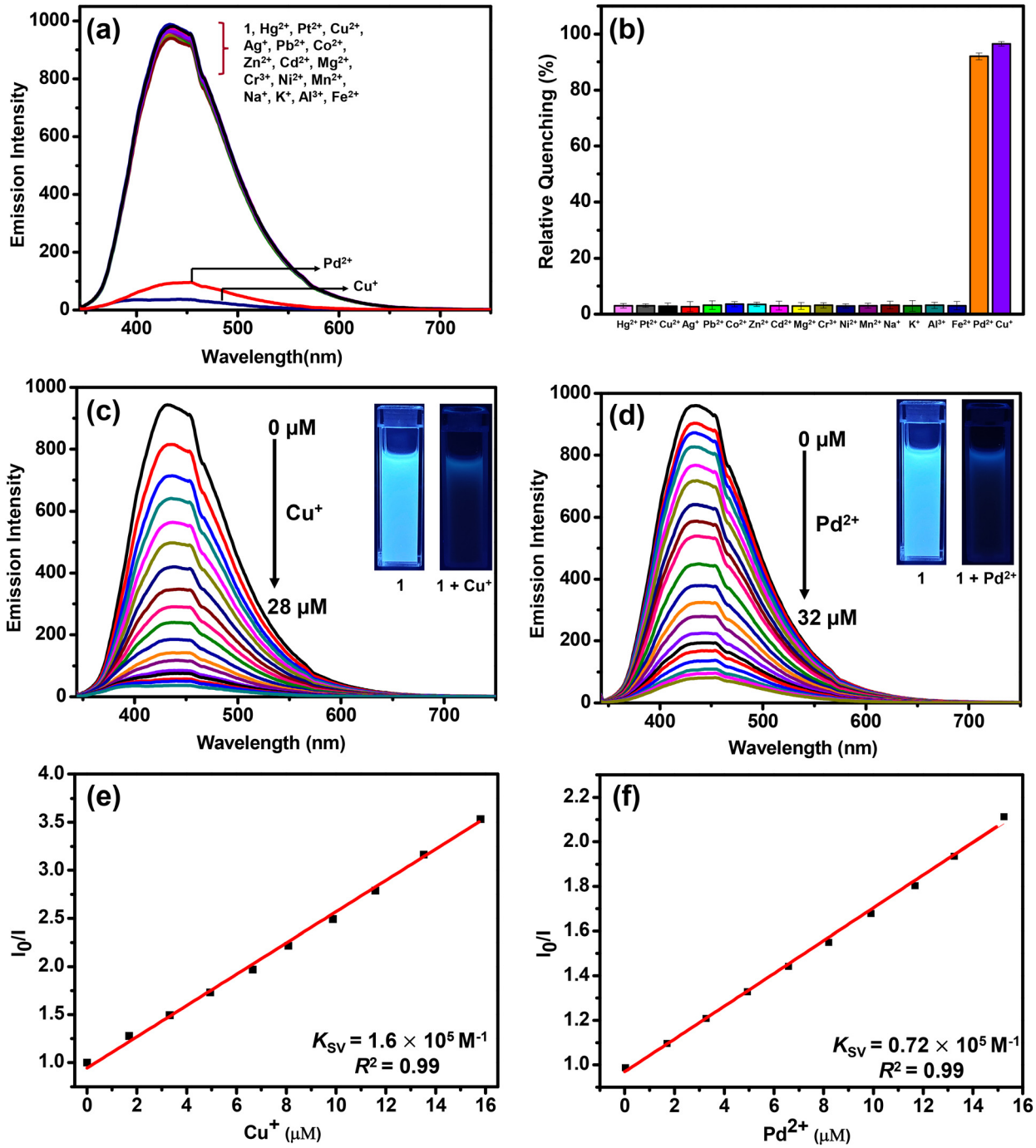


Fig. 2 (a) Change in the emission spectra of MOF **1** in the presence of assorted metal ions (40 μM) in water ($\lambda_{ex}$ = 325 nm). (b) Bar diagram showing relative quenching in the emission intensity of **1** in the presence of assorted metal ions (40 μM). Change in the emission spectra of MOF **1** upon incremental addition of (c) $Cu^{+}$ ions (0–28 μM) and (d) $Pd^{2+}$ ions (0–32 μM). Stern–Volmer plots for the detection of (e) $Cu^{+}$ ions and (f) $Pd^{2+}$ ions by MOF **1**.

 © 2023 The Author(s). Published by the Royal Society of Chemistry

Open Access Article. Published on 06 October 2023. Downloaded on 2/10/2026 7:54:17 PM.
This article is licensed under a Creative Commons Attribution-NonCommercial 3.0 Unported Licence.

**Table 1** Detection parameters for the sensing of $Pd^{2+}$ ions by assorted MOFs reported in the literature

| S. no. | MOF | Solvent | Detection limit (ppb) | Response time (s) | $K_{SV}$ ($M^{-1}$) | Ref. |
|---|---|---|---|---|---|---|
| 1 | Zn-MOF (**1**) | Water | 12.7 | 20 | $0.73 \times 10^5$ | **This work** |
| 2 | $[Al(OH)(L1)]_n$ | Water | 18.1 | 30 | $4.39 \times 10^3$ | 65 |
| 3 | $[Al(OH)(L2)]_n$ | Water | 26.2 | 360 | $1.05 \times 10^5$ | 72 |
| 4 | $[Al(OH)(L3)_{0.54}(L4)_{0.46}]_n$ | Water | 19.5 | 1800 | $1.56 \times 10^4$ | 73 |
| 5 | $[Eu(L5)_{1.5}(DMF)_{0.5}]_n$ | Water | 44 | n.a. | $7.80 \times 10^4$ | 64 |
| 6 | $[Zn(L6)(L7)]_n$ | Water | 35 | n.a. | $4.20 \times 10^4$ | 74 |
| 7 | $[Cd(L6)(L7)]_n$ | Water | 18 | n.a. | $7.90 \times 10^4$ | 74 |
| 8 | $[Zn(L8)_{0.5}(L9)_{0.5}]_n$ | DMF | 30 | n.a. | $3.60 \times 10^4$ | 63 |
| 9 | $[Zn_4O(L10)_3]_n$ | $CH_3CN$ | 500 | 600 | n.a. | 66 |

L1: 5-(prop-2-yn-1-yloxy)isophthalic acid; L2: 5-(allyloxy)isophthalic acid; L3: isophthalic acid; L4: 5-vinylisophthalic acid; L5: 2,5-bis(allyloxy) terephthalic acid; L6: 2-aminoterephthalic acid; L7: (*E*)-*N*′-(pyridin-4-ylmethylene)isonicotinohydrazide; L8: 1,2,4,5-tetrakis(4-carboxyphenyl)benzene; L9: 1,4-bis[2-(4-pyridyl)ethenyl]benzene; L10: 2,5-dithioalloxyterephthalic acid; n.a.: not available.

and $Pd^{2+}$ ions resulted in 96 and 92% quenching in the emission intensity of **1**, respectively (Fig. 2(b)). The emission quenching is assumed to be due to an interaction between the propargyl group of MOF **1** and $Cu^+$ or $Pd^{2+}$ ions (*vide infra*). The higher quenching efficiency observed for the $Cu^+$ ion, compared to the $Pd^{2+}$ ion, is ascribed to its better soft nature due to a lower positive charge which allows it to interact effectively with the propargyl group of **1**.

To further investigate, fluorescence spectral titrations were performed after the sequential addition of solutions of $Cu^+$ and $Pd^{2+}$ ions (2.5 mM) to an aqueous suspension of **1** (Fig. 2(c) and (d)). These titrations allowed us to calculate various binding parameters such as Stern–Volmer constants ($K_{SV}$) (Fig. 2(e) and (f)), binding constants ($K_b$) (Fig. S18, ESI†), and detection limits (Fig. S19, ESI†).[75–77] The Stern–Volmer constants ($K_{SV}$) were found to be $1.6 \times 10^5$ $M^{-1}$ and $0.72 \times 10^5$ $M^{-1}$ for $Cu^+$ and $Pd^{2+}$ ions, respectively. The high values of $K_{SV}$ indicated a strong interaction between **1** and $Cu^+$ and $Pd^{2+}$ ions.[75] The high binding constants of **1** towards $Cu^+$ and $Pd^{2+}$ ions were found to be $5.45 \times 10^4$ $M^{-1}$ and $0.22 \times 10^4$ $M^{-1}$, respectively.[77] Further, MOF **1** showed notable detection limits of 53.05 and 71.53 nM for $Cu^+$ and $Pd^{2+}$ ions, respectively.[76] These detection limits are significantly lower than those of most of the reported MOF-based chemosensors (Table 1).[64–66] In fact, MOFs that can act as chemosensors for the detection of both $Cu^+$ and $Pd^{2+}$ ions are not known. Thus, MOF **1** acted as an efficient and selective chemosensor for the detection of both $Cu^+$ and $Pd^{2+}$ ions in an aqueous medium. Job's plots and mole ratio plots were studied to understand the stoichiometry of the binding event by titrating a suspension of MOF **1** against $Cu^+$ and $Pd^{2+}$ ions and measuring a change in the emission intensity (Fig. S20 and S21, ESI†).[78] Both these methods supported a 1 : 1 stoichiometry of MOF **1** towards both $Cu^+$ and $Pd^{2+}$ ions. To determine the response time of MOF **1** towards $Cu^+$ and $Pd^{2+}$ ions, time-dependent fluorometric titrations were performed.[79] The emission spectra of **1** were recorded at 10 s intervals for up to 2 min. Gratifyingly, within 10 s, the emission intensity of **1** was quenched significantly after the addition of both $Cu^+$ and $Pd^{2+}$ ions (Fig. S22, ESI†). Such a fact illustrates a fast response time of **1** for the sensing of both $Cu^+$ and $Pd^{2+}$ ions compared to other reported MOFs (Table 1).[64–66]

To evaluate the excited state behavior of **1**, time-resolved fluorescence studies were done in the absence and presence of $Cu^+$ and $Pd^{2+}$ ions, respectively (Fig. 3).[80] The lifetime profile of MOF **1** showed a tri-exponential decay with $\tau_{av}$ of 8.43 ns (Table S4†). After the addition of $Cu^+$ and $Pd^{2+}$ ions, the $\tau_{av}$ values decreased to 4.84 ns and 5.06 ns, respectively. These facts suggest strong interaction of $Cu^+$ and $Pd^{2+}$ ions with MOF **1**, probably due to π–d orbitals of the propargyl group and metal ions.[66,67] The said interaction between the fluorophore **1** and quenchers ($Cu^+$ and $Pd^{2+}$) is responsible for the immediate quenching of the fluorophore (*vide infra*).

For many applications, it is highly desirable for a chemosensor to retain its selectivity in the presence of competitive analytes.[76,81] Hence, the selectivity of MOF **1** was assessed towards $Cu^+$ and $Pd^{2+}$ ions in the presence of the following metal ions: $Hg^{2+}$, $Pt^{2+}$, $Cu^{2+}$, $Ag^+$, $Pb^{2+}$, $Co^{2+}$, $Zn^{2+}$, $Cd^{2+}$, $Mg^{2+}$, $Cr^{3+}$, $Ni^{2+}$, $Mn^{2+}$, $Na^+$, $K^+$, $Al^{3+}$, and $Fe^{2+}$ (Fig. S23, ESI†). For such studies, equimolar amounts of $Cu^+$ or $Pd^{2+}$ ions and other competitive metal ions were added to an aqueous suspension of MOF **1**. Notably, none of these metal ions interfered with the detection of both $Cu^+$ and $Pd^{2+}$ ions. Therefore, MOF **1** acts as a highly selective and sensitive chemosensor for the detection of both $Cu^+$ and $Pd^{2+}$ ions

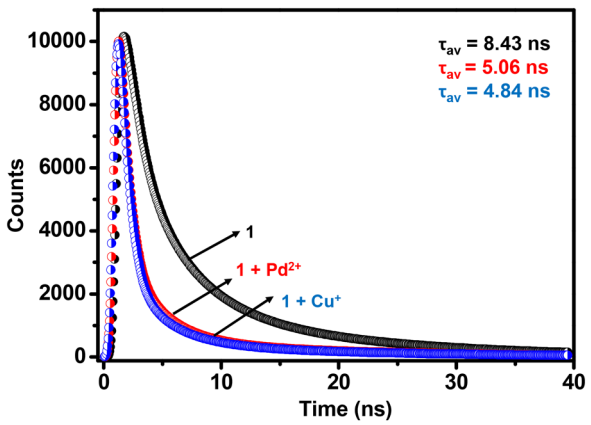


**Fig. 3** Lifetime profiles of MOF **1** in the absence and presence of $Cu^+$ and $Pd^{2+}$ ions in $H_2O$ ($\lambda_{ex}$ = 325 nm).

Open Access Article. Published on 06 October 2023. Downloaded on 2/10/2026 7:54:17 PM.
This article is licensed under a Creative Commons Attribution-NonCommercial 3.0 Unported Licence.

even in the presence of other competitive metal ions. Subsequently, selectivity was studied in the presence of both $Cu^+$ and $Pd^{2+}$ ions. As **1** is noted to bind to both $Cu^+$ and $Pd^{2+}$ ions, as expected, an interference was observed in their presence. With the $Pd^{2+}$ ion, *ca.* 90% quenching was noted; however, further addition of the $Cu^+$ ion led to *ca.* 100% quenching. Similarly, while the $Cu^+$ ion exhibited *ca.* 94% quenching, further addition of the $Pd^{2+}$ ion led to *ca.* 100% quenching.

To evaluate the sensing performance of MOF **1** in the presence of metal salts of different anions, its emission spectra were recorded after the addition of various Cu(I) salts (CuCl, CuSCN, $CuNO_3$ and $[Cu(CH_3CN)_4]ClO_4$) as well as Pd(II) salts ($PdCl_2$, $Pd(OAc)_2$, $Pd(NO_3)_2$ and $PdCl_2(CH_3CN)_2$) (Fig. S24, ESI†). Nearly identical emission quenching illustrates the remarkable efficiency of **1** for the detection of both $Cu^+$ and $Pd^{2+}$ ions across various metal salts with different anions.

### Mechanistic insight

To investigate the mechanism of fluorescence quenching, various experiments were performed. The PXRD patterns of **1** were recorded after its reaction with both $Cu^+$ and $Pd^{2+}$ ions; *i.e.*, **1**-Cu and **1**-Pd (Fig. S25, ESI†). Unnoticeable changes were observed in the PXRD patterns of both **1**-Cu and **1**-Pd when compared to pristine **1**, thus suggesting that emission quenching was not due to any structural change in **1**.[68] In fact, it is important to note that both the structural integrity and stability of **1** remain preserved after sensing experiments. Subsequently, SEM studies were performed to check the morphological stability of **1** after its interaction with $Cu^+$ and $Pd^{2+}$ ions (Fig. S26, ESI†). A nearly identical morphology of **1**, when compared to **1**-Cu and **1**-Pd, confirmed its morphological stability after the detection of $Cu^+$ and $Pd^{2+}$ ions. Thus, the emission quenching of MOF **1** is most probably due to its interaction and/or binding with the analytes ($Cu^+$ and $Pd^{2+}$ ions).

The Stern–Volmer studies were used to interpret the quenching efficiency of **1** towards $Cu^+$ and $Pd^{2+}$ ions. Notably, the Stern–Volmer plots remained linear at all concentrations of $Cu^+$ and $Pd^{2+}$ ions, thus suggesting that either a static or a dynamic quenching pathway is followed during the sensing event.[82] However, the fluorescence lifetime decay profile of **1** displayed significant changes in its lifetime after the addition of $Cu^+$ and $Pd^{2+}$ ions. Such a fact confirms that the emission quenching is not caused by a static but a dynamic quenching pathway *via* energy transfer between the MOF and an analyte. Thus, the mechanism of emission quenching can possibly be ascribed to the strong interaction between the MOF and an analyte accompanied with Förster resonance energy transfer (FRET).[83] Therefore, the lifetime decay studies support the fact that complete complexation has possibly taken place between the propargyl group of MOF **1** and $Cu^+$ or $Pd^{2+}$ ions, which led to FRET between them and thereby emission quenching. FRET is a non-radiative energy transfer process that involves transfer of excitation energy from a donor to an acceptor through dipole–dipole interactions. In order for FRET to take place, there must be a sufficient overlap between the absorption spectrum of an analyte and the emission spectrum of a fluorophore.[84,85] As shown in Fig. 4, the emission band of MOF **1** has a good overlap to the absorption band of $PdCl_2$, thus supporting an efficient energy transfer from **1** (donor) to the $Pd^{2+}$ ion (acceptor). This overlap suggests that the $Pd^{2+}$ ion absorbs the excited state energy of **1** and thus reduces the transfer of energy from the ligand to the $Zn^{2+}$ ion, resulting in emission quenching when **1** interacted with an analyte. Further, the overlap integral ($J_\lambda$) was calculated to evaluate the FRET efficiency between the donor and the acceptor. For the $Pd^{2+}$ ion, the value of $J_\lambda$ was found to be $1.14 \times 10^{14}$ $m^{-1}$ $cm^{-1}$ $nm^4$. A large value of $J_\lambda$ clearly justifies a significant overlap between MOF **1** (donor) and the $Pd^{2+}$ ion (acceptor), which is comparable to many examples available in the literature.[82,84,85] However, similar studies for the $Cu^+$ ion could not be performed as CuCl does not show any absorption band in the visible region.

To further provide evidence of binding between the propargyl group of the MOF and $Cu^+$ or $Pd^{2+}$ ions, the FTIR and solid-state $^{13}C$ NMR spectra of **1**, **1**-Cu and **1**-Pd were studied (Fig. 5).[27] In the FTIR spectra, notable red shifts were observed for both –C≡C–H and –C≡C– stretching of the propargyl group (Fig. S27, ESI†). For **1**-Cu and **1**-Pd, –C≡C–H and –C≡C– stretching were shifted from 3321 to 3311/3309 and from 2122 to 2114/2112 $cm^{-1}$, respectively.[69] Likewise, the solid-state $^{13}C$ NMR spectra (Fig. S28, ESI†) also showed a significant downfield shift in the aliphatic region for both **1**-Cu ($\Delta_\delta$ = 2.13 ppm) and **1**-Pd ($\Delta_\delta$ = 2.03 ppm). It is reasoned that a strong interaction between the π–d orbital of alkyne and metal ions is responsible for such notable deshielding.[86] Subsequently, zeta potentials ($\zeta$) were measured for **1** ($\zeta$ = 0.215) and compared with both **1**-Cu ($\zeta$ = 6.57) and **1**-Pd ($\zeta$ = 6.27) (Fig. S29, ESI†).[87] For both **1**-Cu and **1**-Pd, significant changes in $\zeta$ further support binding of $Cu^+$ and $Pd^{2+}$ ions to the propargyl group of MOF **1**.

Furthermore, X-ray photoelectron spectroscopy (XPS) was used to confirm binding between the propargyl group of MOF **1** and $Cu^+$ and $Pd^{2+}$ ions (Fig. S30, ESI†). In the XPS

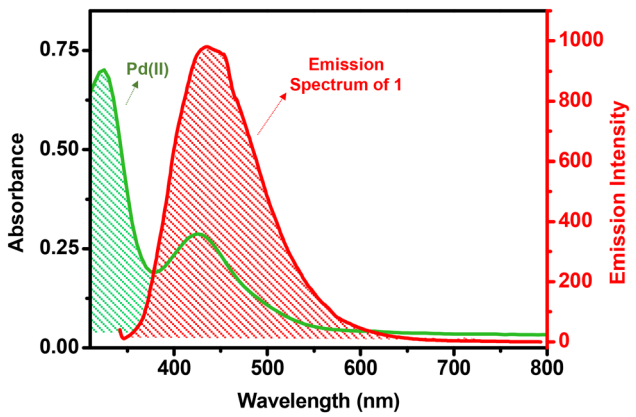


Fig. 4 Spectral overlap between the absorption spectrum of the $Pd^{2+}$ ion and the emission spectrum of MOF **1**.

 © 2023 The Author(s). Published by the Royal Society of Chemistry

Open Access Article. Published on 06 October 2023. Downloaded on 2/10/2026 7:54:17 PM.
This article is licensed under a Creative Commons Attribution-NonCommercial 3.0 Unported Licence.

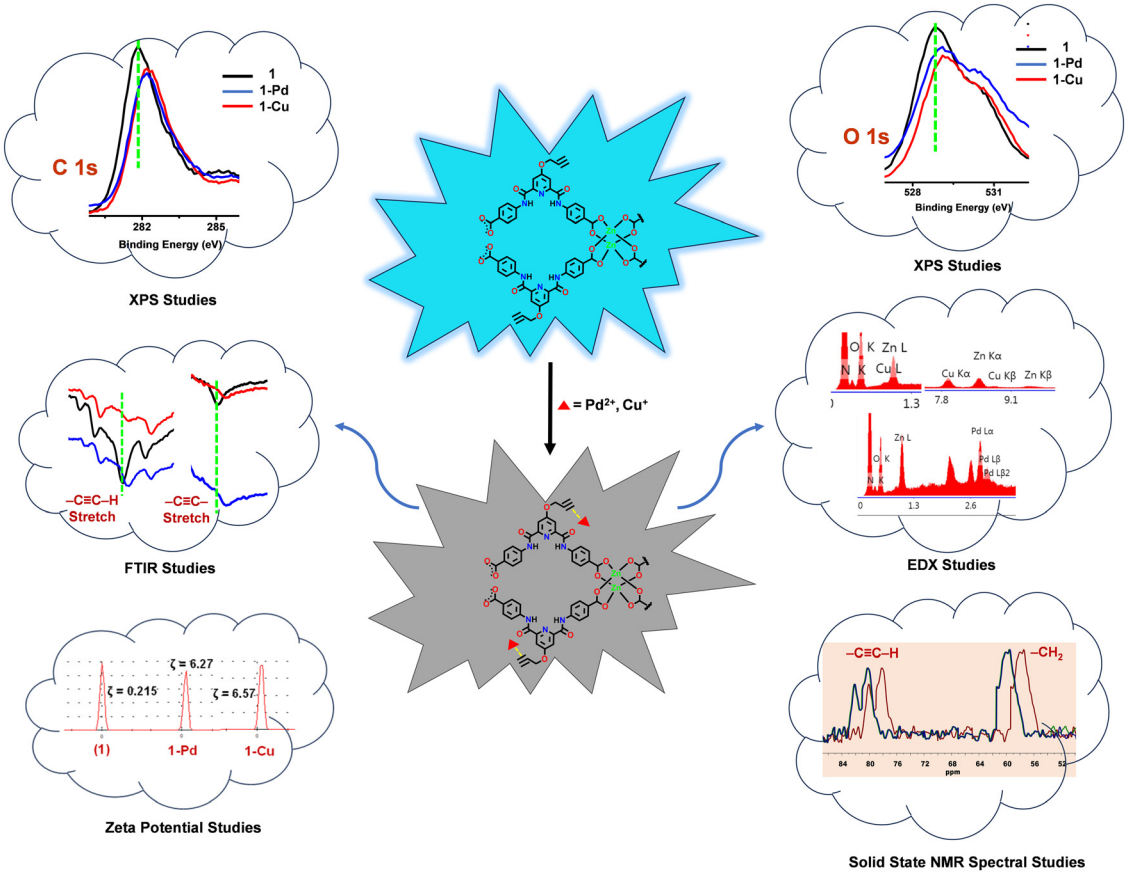


**Fig. 5** The mechanism of detection of $Cu^+$ and $Pd^{2+}$ ions by Zn(II)-MOF **1** using various studies.

spectra, notable shifts were observed in the binding energy (BE) of the C≡C bond and O atom of the propargyl group. For **1**-Cu and **1**-Pd, $BE_{C\equiv C}$ and $BE_{O1s}$ increased by 0.43 and 0.39 eV and 0.31 and 0.29 eV, respectively. Such significant changes in the BE are attributed to the strong interaction between the π-orbitals of the propargyl group and the d-orbitals of $Cu^+$ and $Pd^{2+}$ ions.[65]

In order to further substantiate these findings, EDX analysis was done to confirm the elemental composition of MOF **1** before and after its reaction with $Cu^+$ (**1**-Cu) and $Pd^{2+}$ (**1**-Pd) ions (Fig. S31, ESI†). In both cases, in addition to C, N, O and Zn, EDX analysis also showed the presence of Cu and Pd. Such a fact provides a strong justification about binding between the propargyl group of MOF **1** and the analytes. Collectively, all studies confirm complexation between the $Cu^+$ and $Pd^{2+}$ ions and the propargyl group of the MOF, which resulted in the fluorescence quenching *via* a dynamic quenching pathway.[83]

Finally, in order to substantiate the fact that the tagged propargyl group is indeed responsible for the recognition and binding of both soft metal ions $Cu^+$ and $Pd^{2+}$, we synthesized a novel structural analogue of Zn-MOF **1**. In MOF **2**, the propargyl group was replaced with its reduced chemical analogue, the propyl group. Zn-MOF **2** was synthesized in a similar manner, however, starting with ligand **L5** (Fig. S32–S37, ESI†) bearing a propyl group in place of the propargyl group (Scheme 2). Subsequently, MOF **2** was adequately characterized (Fig. S38 and S39, ESI†) including X-ray diffraction analysis (Tables S5–S7, ESI†).

MOF **2** crystallized in a monoclinic cell with the *P*2/*n* space group. The asymmetric unit consists of one **L5**, one $Zn^{2+}$ ion, one each of a coordinated and a lattice DMSO molecule (Fig. 6(a)). The SBU is composed of four arylcarboxylate groups originating from four different ligands, two Zn(II) ions and two coordinated DMSO molecules, $[Zn_2(-COO)_4(DMSO)_2]$. Every zinc ion exhibits a distorted tetrahedral geometry, and the two zinc atoms are separated by 3.76 Å (Fig. 6(b)). Such SBUs are connected together to form a 3D structure (Fig. 6(c)–(f)).

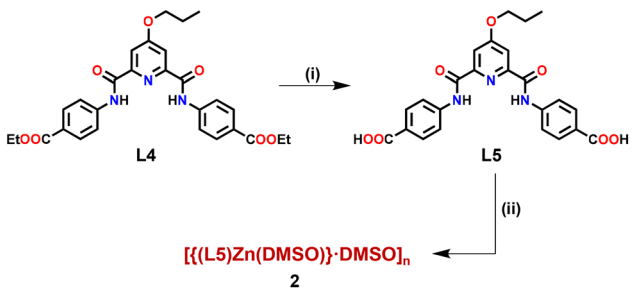


**Scheme 2** Preparative route for the synthesis of Zn(II)-MOF **2**. Conditions: (i) $OH^-$; (ii) $Zn(C_6H_5COO)_2$.

Open Access Article. Published on 06 October 2023. Downloaded on 2/10/2026 7:54:17 PM.
This article is licensed under a Creative Commons Attribution-NonCommercial 3.0 Unported Licence.

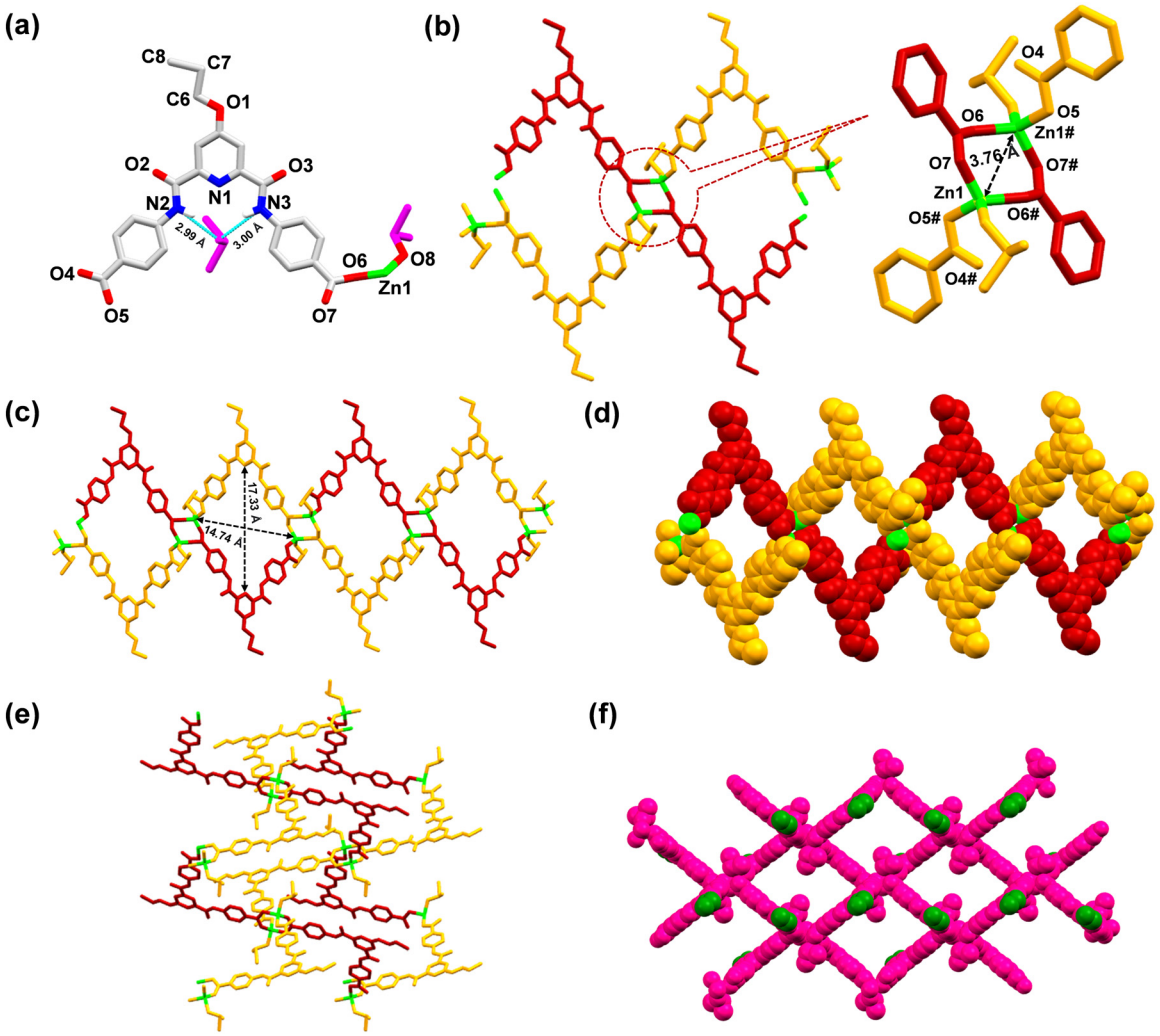


Fig. 6 (a) Asymmetric unit of MOF **2**; colour codes: green, Zn; blue, N; red, O; grey, C; DMSO, pink. The hydrogen atoms, except for the amidic protons, have been omitted for clarity. (b) Partial crystal structure of **2** showing the coordination environment around the $Zn^{2+}$ centers. (c) A view of the 3D network of **2** displaying the cavity structure and its dimensions, when viewed along the *b*-axis. (d) Space-filling diagram of **2**, when viewed along the *b*-axis. (e) A view of the 3D network of **2**, when viewed along the *c*-axis. (f) Space-filling diagram of **2**, where propyl groups are shown in green colour for distinction, when viewed along a perpendicular axis to the *bc* plane.

Similar to MOF **1**, MOF **2** also exhibited the presence of large cavities with dimensions of 17.33 × 14.74 $Å^2$ (Fig. 6(c)). Importantly, the lattice DMSO molecule formed H-bonds (2.99–3.00 Å) with the amidic N–H groups of the ligand and was thus located within the pincer cavity of the MOF.[27,88] The crystal structure of MOF **2**, including its 3D architecture, is very similar to that of MOF **1**, except the tagged propyl group. Such a fact provided an excellent opportunity to evaluate the role of propargyl (MOF **1**) *versus* propyl (MOF **2**) groups in the recognition of both $Cu^+$ and $Pd^{2+}$ ions.

The solid-state fluorescence spectrum of MOF **2** exhibited a prominent emission at 455 nm (Fig. S40, ESI†), while its aqueous suspension also exhibited $\lambda_{em}$ at 455 nm after being excited at 325 nm. The emission spectra of MOF **2**, recorded in a variety of solvents (acetone, MeCN, $CHCl_3$, THF, toluene, MeOH, EtOH, $H_2O$, DMF, DMSO, ethylene glycol, nitrobenzene and nitromethane (Fig. S41, ESI†)), exhibited a comparable spectral response as noted for MOF **1** (Fig. S42, ESI†). Subsequently, the fluorescence spectra of **2** were recorded in the presence of both $Cu^+$ and $Pd^{2+}$ ions in an aqueous medium (Fig. S43, ESI†). Gratifyingly, MOF **2** did not show any response to both $Cu^+$ and $Pd^{2+}$ ions. Such a fact proves the critical role played by the propargyl group in MOF **1** for the detection of these ions. In MOF **1**, the structure included alkyne groups that have the ability to engage in soft interactions with the softer metal ions.[89] Such interactions are crucial for the recognition and binding of soft metal ions, leading to prominent changes in the emission spectrum. In contrast, saturated propyl groups in MOF **2** do not facilitate such interactions, and consequently, **2** is unable to recognize softer metal ions and therefore no quenching is observed for both $Cu^+$ and $Pd^{2+}$ ions. These observations highlight the importance of intricate design in MOF **1** by incorporating alkyne groups that are critical for the detection of soft metal ions through soft–soft interactions.[64,68,89]

 © 2023 The Author(s). Published by the Royal Society of Chemistry

Open Access Article. Published on 06 October 2023. Downloaded on 2/10/2026 7:54:17 PM.
This article is licensed under a Creative Commons Attribution-NonCommercial 3.0 Unported Licence.

### Applications of Zn-MOF 1

**(i) Paper strip-based detection.** To make the detection process convenient, portable and cost-effective, we fabricated MOF-based paper strips for the real-time detection of $Cu^+$ and $Pd^{2+}$ ions (Fig. 7(a)).[90] Such test strips were prepared by soaking paper strips in an aqueous suspension of **1** followed by drying in air. Under UV light, such test strips displayed strong blue fluorescence. However, when such test strips were treated with an aqueous solution of $Cu^+$ and $Pd^{2+}$ ions, the blue emission was fully quenched. Thus, MOF **1** can act as an efficient chemosensor for the detection of $Cu^+$ and $Pd^{2+}$ ions for real-field applications.

**(ii) Detection in different water samples.** To evaluate a wider applicability of MOF **1**, fluorescence studies were performed in different water samples, such as distilled water, tap water, lake water, and river water (Fig. 7(b)).[91] For such studies, suspensions of MOF **1** were prepared in different water samples and emission spectra were recorded in the presence of $Cu^+$ and $Pd^{2+}$ ions. Nearly identical quenching was observed in all water samples. Therefore, MOF **1** is highly efficient for detecting both $Cu^+$ and $Pd^{2+}$ ions in different water samples.

## Conclusions

In conclusion, an alkyne-functionalized Zn(II)-based luminescent MOF (**1**) was synthesized and utilized as an efficient and selective chemosensor for the ultrafast 'turn-off' detection of $Cu^+$ and $Pd^{2+}$ in an aqueous medium. MOF **1** exhibited extremely low nano-molar detection limits for both $Cu^+$ and $Pd^{2+}$ ions with an ultrafast response time. The luminescence quenching of MOF **1** was attributed to FRET as a result of π–d interaction between the alkyne functional group of **1** and $Cu^+$ and $Pd^{2+}$ ions. The mechanism of π–d interaction was inferred with the help of solid-state NMR and FTIR spectral studies, XPS studies, zeta potentials and EDX analyses. To nail, a structural analogue of MOF **1**, MOF **2**, however, carrying a saturated alkyl group, was utilized to confirm the role of the alkyne group in controlling the π–d interaction in **1** and therefore the sensing outcome. This work not only illustrated selective detection of $Cu^+$ and $Pd^{2+}$ ions in aqueous medium but also demonstrated the significant role of incorporating critical functional groups into a MOF structure in achieving selective detection of the targeted analytes.

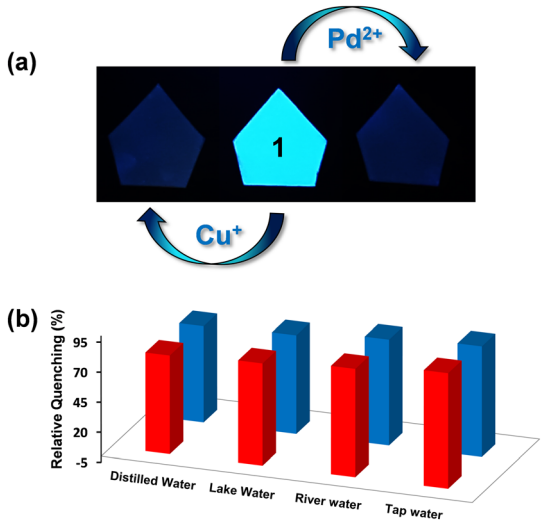


Fig. 7 (a) MOF-coated paper strips in the absence and presence of $Cu^+$ and $Pd^{2+}$ ions under UV light (365 nm) and (b) quenching efficiency of **1** for the $Cu^+$ ion (28 μM, red pillars) and $Pd^{2+}$ ion (32 μM, blue pillars) in various water samples (distilled water, lake water, river water, tap water).

## Syntheses

### Synthesis of L1

**$H_2L^{p\text{-}COOEt}$–OH (L1).** Chelidamic acid (2.00 g, 10.90 mmol) and ethyl 4-aminobenzoate (3.60 g, 21.80 mmol) were taken in 15 mL pyridine and refluxed with stirring for 30 min at 100 °C. To this reaction mixture, triphenyl phosphite (7.45 g, 24.02 mmol) was added dropwise and the reaction mixture was stirred for 8 h at 100 °C. After the reaction mixture was cooled to room temperature, ice-cold water was added, which resulted in instant precipitation of a white product. The white product was filtered, thoroughly washed with water followed by diethyl ether and dried under vacuum. Yield: 4.94 g (95%). $^1$H NMR spectrum (400 MHz, DMSO-$d_6$) $\delta$ 11.73 (s, 1H), 11.12 (s, 2H), 8.06 (d, $J$ = 8.7 Hz, 4H), 7.98 (d, $J$ = 8.6 Hz, 4H), 7.70 (s, 2H), 4.27 (q, $J$ = 7.0 Hz, 4H), 1.29 (t, $J$ = 7.1 Hz, 6H). $^{13}$C NMR spectrum (100 MHz, DMSO-$d_6$) $\delta$ 167.54, 165.84, 162.55, 150.97, 142.96, 130.65, 125.70, 120.67, 113.32, 61.07, 14.74. FTIR spectrum (Zn–Se, selected peaks, $\nu$/cm$^{-1}$): 3450 (O–H), 3288 (N–H), 1696 ($COOCH_2CH_3$), 1585 (C═O). Elemental analysis for $C_{25}H_{23}N_3O_7$: C, 62.89; H, 4.86; N, 8.80. Found: C, 62.62; H, 4.66; N, 8.69.

### Synthesis of L2 and L3

**$H_2L^{p\text{-}COOEt}$–O–$CH_2$–C≡C–H (L2).** **L1** (1.00 g, 2.09 mmol) and propargyl bromide (0.29 g, 2.51 mmol) were dissolved in 20 mL DMF followed by the addition of solid $K_2CO_3$ (0.57 g, 4.18 mmol). The reaction mixture was stirred for 6 h at 60 °C. The unreacted $K_2CO_3$ was filtered off from the reaction mixture and the solvent was removed under reduced pressure. The product was isolated after washing with diethyl ether. Yield: 0.97 g (90%). $^1$H NMR spectrum (400 MHz, DMSO-$d_6$) $\delta$ 11.26 (s, 2H), 8.08 (d, $J$ = 8.7 Hz, 4H), 8.00 (d, $J$ = 8.7 Hz, 4H), 7.92 (s, 2H), 5.13 (s, 2H), 4.28 (q, $J$ = 7.1 Hz, 4H), 3.74 (s, 1H), 1.30 (t, $J$ = 7.1 Hz, 6H). $^{13}$C NMR spectrum (100 MHz, DMSO-$d_6$) $\delta$ 166.72, 165.79, 162.24, 151.16, 142.86, 130.60, 125.79, 120.75, 112.57, 80.43, 78.20, 61.04, 57.07, 14.70. FTIR spectrum (Zn–Se, selected peaks, $\nu$/cm$^{-1}$): 3368 (C≡C–H), 3269 (N–H), 2116 (C≡C), 1688 ($COOCH_2CH_3$), 1596 (C═O). Elemental analysis for $C_{28}H_{25}N_3O_7$: C, 65.24; H, 4.89; N, 8.15. Found: C, 65.15; H, 4.79; N, 8.12.

**$H_2L^{p\text{-}COOH}$–O–$CH_2$–C≡C–H (L3).** Ligand **L3** was obtained after the base-assisted hydrolysis of **L2**. **L2** (0.5 g, 0.96 mmol) was dissolved in a mixture of THF–$H_2O$ (3 : 1, v/v) and treated

Open Access Article. Published on 06 October 2023. Downloaded on 2/10/2026 7:54:17 PM.
This article is licensed under a Creative Commons Attribution-NonCommercial 3.0 Unported Licence.

with 5 equiv. of NaOH (0.19 g, 4.8 mmol). This reaction mixture was stirred for 12 h at room temperature. To this reaction mixture, an aqueous solution of HCl (4 N) was added until the pH reached 3.0–4.0. The resulting solution was vacuum evaporated to remove THF which led to precipitation of a product which was isolated, washed with water, and air dried. Yield: 0.37 g (85%). $^1$H NMR spectrum (400 MHz, DMSO-$d_6$) $\delta$ 12.84 (s, 2H), 11.20 (s, 2H), 8.06 (d, $J$ = 8.6 Hz, 4H), 8.00 (d, $J$ = 8.6 Hz, 4H), 7.93 (s, 2H), 5.15 (s, 2H), 3.56 (s, 1H). $^{13}$C NMR spectrum (100 MHz, DMSO-$d_6$) $\delta$ 167.38, 166.75, 162.12, 151.16, 142.48, 130.81, 126.77, 120.66, 112.53, 80.38, 78.21, 57.05. FTIR spectrum (Zn–Se, selected peaks, $\nu$/cm$^{-1}$): 3365 (C≡C–H), 3280 (N–H), 2134 (C≡C), 1682 (COOH), 1582 (C=O). Elemental analysis for $C_{24}H_{17}N_3O_7$: C, 62.75; H, 3.73; N, 9.15. Found: C, 62.72; H, 3.65; N, 9.09.

### Synthesis of L4 and L5

**$H_2L^{p\text{-}COOEt}$–O–$(CH_2)_2CH_3$ (L4).** **L4** was synthesized using a similar procedure to that mentioned for **L2**, however, using the following reagents: **L1** (1.00 g, 2.09 mmol), propyl bromide (0.3 g, 2.51 mmol) and $K_2CO_3$ (0.57 g, 4.18 mmol). Yield: 0.95 g (88%). $^1$H NMR spectrum (400 MHz, DMSO-$d_6$) $\delta$ 11.28 (s, 2H), 8.12 (d, $J$ = 8.8 Hz, 4H), 8.03 (d, $J$ = 8.8 Hz, 4H), 7.85 (s, 2H), 4.32 (q, $J$ = 7.1 Hz, 4H), 4.24 (t, $J$ = 6.4 Hz, 2H), 1.88–1.76 (m, 2H), 1.34 (t, $J$ = 7.1 Hz, 6H), 1.02 (t, $J$ = 7.4 Hz, 3H). $^{13}$C NMR spectrum (100 MHz, DMSO-$d_6$) $\delta$ 167.99, 165.79, 162.79, 151.12, 142.89, 130.58, 125.75, 120.72, 112.09, 64.89, 61.02, 22.12, 14.70, 10.65. FTIR spectrum (Zn–Se, selected peaks, $\nu$/cm$^{-1}$): 3349 (N–H), 2980 (C–H), 1697 ($COOCH_2CH_3$), 1582 (C=O). Elemental analysis for $C_{28}H_{29}N_3O_7$: C, 64.73; H, 5.63; N, 8.09. Found: C, 64.55; H, 5.60; N, 8.22.

**$H_2L^{p\text{-}COOH}$–O–$(CH_2)_2CH_3$ (L5).** Ligand **L5** was synthesized using a similar procedure to that mentioned for **L3**, however, using **L4**. Yield: 0.36 g (82%). $^1$H NMR spectrum (400 MHz, DMSO-$d_6$) $\delta$ 12.85 (s, 2H), 11.19 (s, 2H), 8.08 (d, $J$ = 8.6 Hz, 4H), 8.03 (d, $J$ = 8.6 Hz, 4H), 7.84 (s, 2H), 4.23 (t, $J$ = 6.3 Hz, 2H), 1.82–1.79 (m, 2H), 1.02 (t, $J$ = 7.4 Hz, 2H). $^{13}$C NMR spectrum (100 MHz, DMSO-$d_6$) $\delta$ 168.01, 167.39, 162.24, 151.09, 142.50, 130.77, 126.78, 120.58, 112.01, 70.70, 22.12, 10.63. FTIR spectrum (Zn–Se, selected peaks, $\nu$/cm$^{-1}$): 3342 (N–H), 2953 (C–H), 1682 (COOH), 1580 (C=O). Elemental analysis for $C_{24}H_{21}N_3O_7$: C, 62.20; H, 4.57; N, 9.07. Found: C, 61.98; H, 4.40; N, 9.15.

### Synthesis of Zn(II) MOFs

**$[\{(L3)Zn\}\cdot H_2O\cdot DMSO]_n$ (1).** An aqueous solution of $Zn(OAc)_2\cdot 2H_2O$ (95.55 mg, 0.43 mmol) was layered over a DMSO solution of **L3** (100.00 mg, 0.21 mmol) with an intermediate layer of *tert*-butanol. After a period of 8–10 days, colourless needle-shaped crystals were obtained, which were filtered, washed with diethyl ether, and dried under vacuum. Yield: 130.00 mg (70%). FTIR spectrum (Zn–Se, selected peaks, $\nu$/cm$^{-1}$): 3321 (C≡C–H), 3284 (N–H), 2122 (C≡C), 1675, 1589 (C=O). Elemental analysis for $C_{26}H_{23}N_3O_{12}SZn_4$: C, 36.18; H, 2.69; N, 4.87; S, 3.71. Found: C, 36.02; H, 2.75; N, 4.98; S, 3.67.

**$[\{(L5)Zn(DMSO)\}\cdot DMSO]_n$ (2).** A MeOH solution of $Zn(C_6H_5COO)_2$ (133 mg, 0.43 mmol) was layered over a DMSO solution of **L5** (100.00 mg, 0.21 mmol) with an intermediate layer of *tert*-butanol. After a period of 7–9 days, colourless block-shaped crystals were obtained, which were filtered, washed with diethyl ether, and dried under vacuum. Yield: 131.00 mg (72%). FTIR spectrum (Zn–Se, selected peaks, $\nu$/cm$^{-1}$): 3241 (N–H), 2961 (C–H), 1675, 1603 (C=O). Elemental analysis for $C_{28}H_{31}N_3O_{11}S_2Zn_3$: C, 39.76; H, 3.69; N, 4.97; S, 7.58. Found: C, 39.56; H, 3.55; N, 4.85; S, 7.53.

## Author contributions

Conceptualization: AA and RaG. Methodology: AA and RuG. Writing – original draft: AA and RaG. Supervision: RaG. Funding acquisition: RaG. The manuscript was written through contributions of all authors. All authors have given approval to the final version of the manuscript.

## Conflicts of interest

The authors declare no competing financial interest.

## Acknowledgements

RaG gratefully acknowledges financial support from the Science & Engineering Research Board, New Delhi, India (CRG/2021/001700). AA and RuG thank CSIR, New Delhi, India for their SRF fellowships. The authors thank USIC at this university for the instrumental facilities and Prof. P. Venkatesu for the $\zeta$-potential measurements.

## Notes and references

1 W. P. Lustig, S. Mukherjee, N. D. Rudd, A. V. Desai, J. Li and S. K. Ghosh, *Chem. Soc. Rev.*, 2017, **46**, 3242–3285.
2 Z. Zhang, H. T. H. Nguyen, S. A. Miller, A. M. Ploskonka, J. B. DeCoste and S. M. Cohen, *J. Am. Chem. Soc.*, 2016, **138**, 920–925.
3 G. Kumar and R. Gupta, *Chem. Soc. Rev.*, 2013, **42**, 9403.
4 Y. Cui, J. Zhang, H. He and G. Qian, *Chem. Soc. Rev.*, 2018, **47**, 5740–5785.
5 C. Jiang, X. Wang, Y. Ouyang, K. Lu, W. Jiang, H. Xu, X. Wei, Z. Wang, F. Dai and D. Sun, *Nanoscale Adv.*, 2022, **4**, 2077–2089.
6 K. Nath, A. Ahmed, D. J. Siegel and A. J. Matzger, *J. Am. Chem. Soc.*, 2022, **144**, 20939–20946.
7 B. Li, H.-M. Wen, W. Zhou and B. Chen, *J. Phys. Chem. Lett.*, 2014, **5**, 3468–3479.
8 Y. Ye, S. Xian, H. Cui, K. Tan, L. Gong, B. Liang, T. Pham, H. Pandey, R. Krishna, P. C. Lan, K. A. Forrest, B. Space, T. Thonhauser, J. Li and S. Ma, *J. Am. Chem. Soc.*, 2022, **144**, 1681–1689.
9 M. Sadakiyo, H. Kasai, K. Kato, M. Takata and M. Yamauchi, *J. Am. Chem. Soc.*, 2014, **136**, 1702–1705.

 © 2023 The Author(s). Published by the Royal Society of Chemistry

Open Access Article. Published on 06 October 2023. Downloaded on 2/10/2026 7:54:17 PM.
This article is licensed under a Creative Commons Attribution-NonCommercial 3.0 Unported Licence.

10 D.-W. Lim and H. Kitagawa, *Chem. Rev.*, 2020, **120**, 8416–8467.
11 L. E. Kreno, K. Leong, O. K. Farha, M. Allendorf, R. P. Van Duyne and J. T. Hupp, *Chem. Rev.*, 2012, **112**, 1105–1125.
12 A. Mallick, A. M. El-Zohry, O. Shekhah, J. Yin, J. Jia, H. Aggarwal, A.-H. Emwas, O. F. Mohammed and M. Eddaoudi, *J. Am. Chem. Soc.*, 2019, **141**, 7245–7249.
13 F. D. Duman and R. S. Forgan, *J. Mater. Chem. B*, 2021, **9**, 3423–3449.
14 S. Horike, N. Ma, Z. Fan, S. Kosasang and M. M. Smedskjaer, *Nano Lett.*, 2021, **21**, 6382–6390.
15 A. Bavykina, N. Kolobov, I. S. Khan, J. A. Bau, A. Ramirez and J. Gascon, *Chem. Rev.*, 2020, **120**, 8468–8535.
16 G. Kumar, F. Hussain and R. Gupta, *Dalton Trans.*, 2017, **46**, 15023–15031.
17 G. Kumar, F. Hussain and R. Gupta, *Dalton Trans.*, 2018, **47**, 16985–16994.
18 L.-F. Wang, W.-M. Zhuang, G.-Z. Huang, Y.-C. Chen, J.-Z. Qiu, Z.-P. Ni and M.-L. Tong, *Chem. Sci.*, 2019, **10**, 7496–7502.
19 H.-C. Zhou, J. R. Long and O. M. Yaghi, *Chem. Rev.*, 2012, **112**, 673–674.
20 D. Kim, X. Liu and M. S. Lah, *Inorg. Chem. Front.*, 2015, **2**, 336–360.
21 W. Lu, Z. Wei, Z.-Y. Gu, T.-F. Liu, J. Park, J. Park, J. Tian, M. Zhang, Q. Zhang, T. G. Iii, M. Bosch and H.-C. Zhou, *Chem. Soc. Rev.*, 2014, **43**, 5561–5593.
22 A. E. Baumann, D. A. Burns, B. Liu and V. S. Thoi, *Commun. Chem.*, 2019, **2**, 1–14.
23 H.-Y. Li, S.-N. Zhao, S.-Q. Zang and J. Li, *Chem. Soc. Rev.*, 2020, **49**, 6364–6401.
24 B.-L. Hou, D. Tian, J. Liu, L.-Z. Dong, S.-L. Li, D.-S. Li and Y.-Q. Lan, *Inorg. Chem.*, 2016, **55**, 10580–10586.
25 L. Li, S. Shen, R. Lin, Y. Bai and H. Liu, *Chem. Commun.*, 2017, **53**, 9986–9989.
26 W. Liu, Y. Wang, Z. Bai, Y. Li, Y. Wang, L. Chen, L. Xu, J. Diwu, Z. Chai and S. Wang, *ACS Appl. Mater. Interfaces*, 2017, **9**, 16448–16457.
27 G. Kumar, S. Pachisia, P. Kumar, V. Kumar and R. Gupta, *Chem. – Asian J.*, 2019, **14**, 4594–4600.
28 S.-S. Zhao, J. Yang, Y.-Y. Liu and J.-F. Ma, *Inorg. Chem.*, 2016, **55**, 2261–2273.
29 Z. Hu, B. J. Deibert and J. Li, *Chem. Soc. Rev.*, 2014, **43**, 5815–5840.
30 S. S. Nagarkar, T. Saha, A. V. Desai, P. Talukdar and S. K. Ghosh, *Sci. Rep.*, 2014, **4**, 7053.
31 M. SK, S. Banesh, V. Trivedi and S. Biswas, *Inorg. Chem.*, 2018, **57**, 14574–14581.
32 Y. Li, M. Sun, Y. Yang, H. Meng, Q. Wang, C. Li and G. Li, *J. Mater. Chem. C*, 2021, **9**, 8683–8693.
33 D. C. Crans and K. Kostenkova, *Commun. Chem.*, 2020, **3**, 1–4.
34 K. P. Carter, A. M. Young and A. E. Palmer, *Chem. Rev.*, 2014, **114**, 4564–4601.
35 A. T. Aron, K. M. Ramos-Torres, J. A. Cotruvo and C. J. Chang, *Acc. Chem. Res.*, 2015, **48**, 2434–2442.
36 J. Joseph, A. Cotruvo, A. T. Aron, K. M. Ramos-Torres and C. J. Chang, *Chem. Soc. Rev.*, 2015, **44**, 4400–4414.
37 S. Puig and D. J. Thiele, *Curr. Opin. Chem. Biol.*, 2002, **6**, 171–180.
38 P. Verwilst, K. Sunwoo and J. S. Kim, *Chem. Commun.*, 2015, **51**, 5556–5571.
39 A. Farhi, F. Firdaus, H. Saeed, A. Mujeeb, M. Shakir and M. Owais, *Photochem. Photobiol. Sci.*, 2019, **18**, 3008–3015.
40 J. Chen, H. Chen, T. Wang, J. Li, J. Wang and X. Lu, *Anal. Chem.*, 2019, **91**, 4331–4336.
41 J.-C. Jin, J. Wu, G.-P. Yang, Y.-L. Wu and Y.-Y. Wang, *Chem. Commun.*, 2016, **52**, 8475–8478.
42 J. Hou, P. Jia, K. Yang, T. Bu, S. Zhao, L. Li and L. Wang, *ACS Appl. Mater. Interfaces*, 2022, **14**, 13848–13857.
43 L.-L. Liu, Y.-Z. Yu, X.-J. Zhao, Y.-R. Wang, F.-Y. Cheng, M.-K. Zhang, J.-J. Shu and L. Liu, *Dalton Trans.*, 2018, **47**, 7787–7794.
44 R. Chinchilla and C. Nájera, *Chem. Rev.*, 2007, **107**, 874–922.
45 T. Iwasawa, M. Tokunaga, Y. Obora and Y. Tsuji, *J. Am. Chem. Soc.*, 2004, **126**, 6554–6555.
46 H. Li, J. Fan and X. Peng, *Chem. Soc. Rev.*, 2013, **42**, 7943–7962.
47 M. Lafrance and K. Fagnou, *J. Am. Chem. Soc.*, 2006, **128**, 16496–16497.
48 X.-F. Wu, H. Neumann and M. Beller, *Chem. Soc. Rev.*, 2011, **40**, 4986–5009.
49 T. Z. Liu, S. D. Lee and R. S. Bhatnagar, *Toxicol. Lett.*, 1979, **4**, 469–473.
50 J. C. Wataha and C. T. Hanks, *J. Oral Rehabil.*, 1996, **23**, 309–320.
51 J. Kielhorn, C. Melber, D. Keller and I. Mangelsdorf, *Int. J. Hyg. Environ. Health*, 2002, **205**, 417–432.
52 C. Melber, D. Keller, I. Mangelsdorf and I. P. on C. Safety, *Palladium*, World Health Organization, 2002.
53 X. Tian, L. C. Murfin, L. Wu, S. E. Lewis and T. D. James, *Chem. Sci.*, 2021, **12**, 3406–3426.
54 L. Basabe-Desmonts, D. N. Reinhoudt and M. Crego-Calama, *Chem. Soc. Rev.*, 2007, **36**, 993–1017.
55 S. Wang, H. Li, H. Huang, X. Cao, X. Chen and D. Cao, *Chem. Soc. Rev.*, 2022, **51**, 2031–2080.
56 O. Knopfmacher, M. L. Hammock, A. L. Appleton, G. Schwartz, J. Mei, T. Lei, J. Pei and Z. Bao, *Nat. Commun.*, 2014, **5**, 2954.
57 A. Kaushik, R. Kumar, S. K. Arya, M. Nair, B. D. Malhotra and S. Bhansali, *Chem. Rev.*, 2015, **115**, 4571–4606.
58 B. Yan, *Inorg. Chem. Front.*, 2021, **8**, 201–233.
59 I. A. Revesz, S. M. Hickey and M. J. Sweetman, *J. Mater. Chem. B*, 2022, **10**, 4346–4362.
60 M. J. Molaei, *Anal. Methods*, 2020, **12**, 1266–1287.
61 X.-G. Liu, H. Wang, B. Chen, Y. Zou, Z.-G. Gu, Z. Zhao and L. Shen, *Chem. Commun.*, 2015, **51**, 1677–1680.
62 Y. Shu, Q. Ye, T. Dai, Q. Xu and X. Hu, *ACS Sens.*, 2021, **6**, 641–658.
63 S. Sanda, S. Parshamoni, S. Biswas and S. Konar, *Chem. Commun.*, 2015, **51**, 6576–6579.

Open Access Article. Published on 06 October 2023. Downloaded on 2/10/2026 7:54:17 PM.
This article is licensed under a Creative Commons Attribution-NonCommercial 3.0 Unported Licence.

64 A. Helal, H. L. Nguyen, A. Al-Ahmed, K. E. Cordova and Z. H. Yamani, *Inorg. Chem.*, 2019, **58**, 1738–1741.
65 P. Chakraborty, A. Rana, S. Mukherjee and S. Biswas, *Inorg. Chem.*, 2023, **62**, 802–809.
66 J. He, M. Zha, J. Cui, M. Zeller, A. D. Hunter, S.-M. Yiu, S.-T. Lee and Z. Xu, *J. Am. Chem. Soc.*, 2013, **135**, 7807–7810.
67 B. M. Trost, M. T. Sorum, C. Chan and G. Rühter, *J. Am. Chem. Soc.*, 1997, **119**, 698–708.
68 P. Samanta, A. V. Desai, S. Sharma, P. Chandra and S. K. Ghosh, *Inorg. Chem.*, 2018, **57**, 2360–2364.
69 K. Nakamoto, *Infrared and Raman Spectra of Inorganic and Coordination Compounds: Part A: Theory and Applications in Inorganic Chemistry*, 6th edn, 2008.
70 F. Ambroz, T. J. Macdonald, V. Martis and I. P. Parkin, *Small Methods*, 2018, **2**, 1800173.
71 X. Liu, X. Wang and F. Kapteijn, *Chem. Rev.*, 2020, **120**, 8303–8377.
72 S. Ghosh, F. Steinke, A. Rana, M. Alam and S. Biswas, *Eur. J. Inorg. Chem.*, 2021, **2021**, 3846–3851.
73 S. Nandi, H. Reinsch and S. Biswas, *Microporous Mesoporous Mater.*, 2020, **293**, 109790.
74 B. Parmar, Y. Rachuri, K. K. Bisht and E. Suresh, *Inorg. Chem.*, 2017, **56**, 10939–10949.
75 D. Prabha, D. Singh, P. Kumar and R. Gupta, *Inorg. Chem.*, 2021, **60**, 17889–17899.
76 V. Kumar, P. Kumar, S. Kumar, D. Singhal and R. Gupta, *Inorg. Chem.*, 2019, **58**, 10364–10376.
77 H. A. Benesi and J. H. Hildebrand, *J. Am. Chem. Soc.*, 1949, **71**, 2703–2707.
78 F. Ulatowski, K. Dąbrowa, T. Bałakier and J. Jurczak, *J. Org. Chem.*, 2016, **81**, 1746–1756.
79 D. Singh, S. Tomar, S. Singh, G. Chaudhary, A. P. Singh and R. Gupta, *J. Photochem. Photobiol., A*, 2023, **435**, 114334.
80 J. S. Buterbaugh, J. P. Toscano, W. L. Weaver, J. R. Gord, C. M. Hadad, T. L. Gustafson and M. S. Platz, *J. Am. Chem. Soc.*, 1997, **119**, 3580–3591.
81 K. Sasakura, K. Hanaoka, N. Shibuya, Y. Mikami, Y. Kimura, T. Komatsu, T. Ueno, T. Terai, H. Kimura and T. Nagano, *J. Am. Chem. Soc.*, 2011, **133**, 18003–18005.
82 A. S. Tanwar, R. Parui, R. Garai, M. A. Chanu and P. K. Iyer, *ACS Meas. Sci. Au*, 2022, **2**, 23–30.
83 B. Sarkar, K. Ishii and T. Tahara, *J. Phys. Chem. Lett.*, 2019, **10**, 5536–5541.
84 X. Jiang, J. Zhang, R. Fan, X. Zhou, K. Zhu and Y. Yang, *ACS Appl. Mater. Interfaces*, 2022, **14**, 49945–49956.
85 P. Rani, Gauri, A. Husain, K. K. Bhasin and G. Kumar, *Cryst. Growth Des.*, 2020, **20**, 7141–7151.
86 Y.-X. Tan, J. Lin, Q.-H. Li, L. Li, R. Anil Borse, W. Lu, Y. Wang and D. Yuan, *Angew. Chem.*, 2023, **135**, e202302882.
87 R. Gupta, G. Kumar and R. Gupta, *Inorg. Chem.*, 2022, **61**, 7682–7699.
88 S. Pachisia, R. Gupta and R. Gupta, *Inorg. Chem.*, 2022, **61**, 3616–3630.
89 H. E. Skipper, C. V. May, A. L. Rheingold, L. H. Doerrer and M. Kamenetska, *J. Am. Chem. Soc.*, 2021, **143**, 16439–16447.
90 B. Wang, X.-L. Lv, D. Feng, L.-H. Xie, J. Zhang, M. Li, Y. Xie, J.-R. Li and H.-C. Zhou, *J. Am. Chem. Soc.*, 2016, **138**, 6204–6216.
91 F. M. Ebrahim, T. N. Nguyen, S. Shyshkanov, A. Gładysiak, P. Favre, A. Zacharia, G. Itskos, P. J. Dyson and K. C. Stylianou, *J. Am. Chem. Soc.*, 2019, **141**, 3052–3058.

 © 2023 The Author(s). Published by the Royal Society of Chemistry